Journal of Engineering Mathematics **32:** 121–142, 1997.

Direct numerical simulation of supersonic jet flow

K. H. LUO and N. D. SANDHAM
Department of Engineering, Queen Mary and Westfield College, University of London, London E1 4NS, U.K.

Received 5 November 1996; accepted in revised form 2 February 1997

Abstract. A numerical method is given for direct numerical simulation of the nonlinear evolution of instability waves in supersonic round jets, with spatial discretisation based on high-order compact finite differences. The numerical properties of a class of symmetric and asymmetric schemes are analysed. Implementation for the Navier–Stokes equations in cylindrical polar coordinates is discussed with particular attention given to treatment of the origin to ensure stability and efficiency. Validation of the schemes is carried out by detailed comparison with linear stability theory. The computer code is applied to study the initial stages of nonlinear development of unstable modes in a Mach 3 jet. The modes of instability that are present include strongly unstable axisymmetric acoustic and helical vortical waves, as well as weakly unstable radiating acoustic and vortical modes. Three distinctive wave patterns are observed from the simulations including a cross-hatched internal shock structure. Nonlinear interactions between the vortical and acoustic modes are investigated.

Key words: DNS, jets, supersonics, finite differences, shocks.

1. Introduction

Direct numerical simulation (DNS) of fluid flow provides detailed information about turbulence which can be used to validate simpler models. Lele [1] gives a review of advances in the study of compressible turbulence, emphasising results from simulations of isotropic and homogeneous flows. DNS has also been used to good effect in the study of a simple plane mixing layer, which is a prototype flow for the early stages of development of a jet. Early direct numerical simulations (Sandham and Reynolds [2]) showed an important compressibility effect to be the breakdown of the spanwise roller structure that is seen to dominate experiments at low Mach numbers. Further work (Vreman *et al.* [3]) used turbulence statistics from DNS databases to prove that the reduction in growth rate of the mixing layer with Mach number was due to a reduction in the magnitude of pressure fluctuations rather than an explicit compressibility term in the Reynolds-averaged equations. This has the important implication for turbulence modelling that the pressure-strain term is the main contributor to compressibility effects.

In this paper we consider the supersonic round jet, which has been the subject of several experimental and theoretical studies in the past. Three families of instability waves in Mach 2 jets were observed in the experiments of Oertel [4, 5]. Later, Tam and Hu [6] identified them as Kelvin–Helmholtz, supersonic and subsonic instability waves using linear stability analysis based on a vortex-sheet model. Similar instabilities were found by Mack [7], again using linear stability analysis, but with a piecewise mean profile to get finite mixing-layer thickness. Mack divided the instability waves into two families: vorticity modes and acoustic modes. He predicted that acoustic modes exist whenever there is an embedded region of locally supersonic flow relative to the phase speed of the instability wave. Questions about the nonlinear development of instabilities and the relation to turbulence structure in the fully-developed jet have not been explored in the previous work.

A variety of numerical problems appear when we consider carrying out a DNS of the supersonic round jet. In common with the mixing layer there is a need to resolve a wide range of turbulent length scales. Spectral or high-order compact schemes have been the favoured methods to solve this problem in the past. In addition we are interested in the sound generated from eddies in the jets, and so it is necessary to resolve waves emanating from the jet and travelling out through the near sound field. An extra physical feature of the supersonic jet flow is the presence of an enclosed region of flow that is supersonic relative to the external flow, giving the extra Mack modes of instability. We may reduce the cost of numerical simulations of the early nonlinear development of instabilities by working in a cylindrical polar-coordinate system, and only retaining a relatively small number of modes in the azimuthal direction. This introduces the potential problem of the coordinate singularity at the origin. Also, since all direct simulations of the compressible equations use explicit methods, there is a problem of small cell sizes near the origin leading to impractically small time steps for stability.

We have to consider the problem of shock waves when devising a numerical scheme to be applied for supersonic flow. Shock capturing schemes (*e.g.* Total Variation Diminishing or Essentially Non-Oscillatory schemes), originally developed for calculations of strong shock waves using the Euler equations, are generally too expensive to implement over the whole computational domain for DNS. Shock waves generated by the turbulence itself (eddy-shocklets) may be weak enough to be resolved with a non-dissipative scheme. Stronger eddy-shocklets need the introduction of additional dissipation into the numerical scheme or the specification of a scheme that automatically switches to a shock-capturing method whenever strong shocks are present. Examples of the latter approach are the schemes of Vreman *et al.* [8] and Adams and Shariff [9].

The present paper is organised as follows. In Section 2 we provide numerical details, including analysis of a class of upwind compact schemes requiring only a tridiagonal matrix solution, and a multidomain approach to limit the time-step restriction near the origin of the co-ordinate system. In Section 3 we tackle the issue of code validation by solving the compressible linear stability problem for the round supersonic jet and comparing the growth rates with simulations. Results from simulations into the nonlinear evolution of instability waves are given in Section 4, with conclusions in Section 5.

2. Numerical methods

The three-dimensional time-dependent compressible Navier–Stokes equations in cylindrical coordinates are shown in Appendix A. These equations plus a scalar transport equation are solved in a moving frame that convects with a characteristic speed of large-scales in a round jet. Fourier spectral methods are used for the periodic azimuthal (θ) and axial (z) directions. In the non-periodic radial direction, two types of high-order compact finite-difference schemes are used. The first is a 6th-order symmetric scheme developed by Lele [10], which has been well tested in a wide range of applications [2, 11, 12]. It is denoted by SCS643, since the next-to-boundary scheme is of 4th-order and the boundary scheme is of 3rd-order accuracy. The second type is a class of asymmetric compact schemes that are to be developed in the following section. Since open-space boundaries are specified in the radial direction, spurious wave reflections at the boundaries need to be prevented. The characteristic non-reflecting boundary conditions originally developed by Thompson [13] are adapted for the present case of cylindrical coordinates. Time advance is performed with a 3rd-order compact-storage Runge–Kutta method.

2.1. ASYMMETRIC COMPACT SCHEMES

We consider a class of compact finite difference schemes of the following formulation

$$f'_{j-1} + Af'_j + \sigma f'_{j+1} = \frac{1}{h}(Bf_{j-2} + Cf_{j-1} + Df_j + Ef_{j+1} + Ff_{j+2}) \tag{1}$$

on a uniformly discretised domain [0, 1] with nodes $x_j = jh$ for $j = 0, 1, \ldots, N-1$. The function values at the nodes are f_j and the finite-difference approximations to the first derivatives are f'_j. An asymmetry parameter σ is introduced to make the scheme upwind-biased. When $\sigma = 1$, it reduces to the symmetric scheme described by Lele [10]. When $\sigma \neq 1$, numerical dissipation is introduced at high wavenumbers, as will be shown later. This scheme is different from that of Adams and Shariff [9] in that it only requires the solution of a tridiagonal matrix system and has explicit control on the amount of numerical dissipation introduced. The general formulation of Adams and Shariff [9] usually requires complex mathematics to determine the unknown coefficients and to solve the resulting matrices that are typically pentadiagonal. The unknown coefficients A to F in Equation (1) are to be related directly to the asymmetry parameter σ. These are determined in such a way that the highest possible order of accuracy is obtained. We achieve this by first expanding all the functions in Equation (1) in Taylor series and then setting as many as possible the resulting Taylor-series coefficients to zero. This gives a set of linear equations from which the coefficients A to F are found

$$\begin{aligned} A &= \frac{3(\sigma+1)}{2}, \qquad B = \frac{\sigma-3}{24}, \qquad C = \frac{-(3\sigma+11)}{6}, \\ D &= \frac{3(-\sigma+1)}{2}, \qquad E = \frac{11\sigma+3}{3}, \qquad F = \frac{3\sigma-1}{24}. \end{aligned} \tag{2}$$

The truncation error is determined by the first nonzero term in the resulting Taylor series, which in the above case is $\varepsilon = [(1-\sigma)/120]h^5 f^{(6)}$. As can be seen, when $\sigma \neq 1$, the compact scheme is of 5th-order accuracy. When $\sigma = 1$, it is of 6th-order, which is the same as derived by Lele [10].

For periodic problems, the above scheme can be applied directly and the formal accuracy is maintained. For non-periodic problems, the inner scheme as derived above must be supplemented by boundary schemes. Inevitably, boundary schemes are asymmetric. Furthermore, it has been shown that in order to preserve a global nth-order formal accuracy (of the inner scheme), the boundary scheme must be of no less than $(n-1)$th-order [14]. For the 5th-order scheme in (1), a suitable boundary scheme of 4th order is given by [10]

$$f'_1 + 3f'_2 = \frac{1}{h}(-\tfrac{17}{6}f_1 + \tfrac{3}{2}f_2 + \tfrac{3}{2}f_3 - \tfrac{1}{6}f_4), \tag{3}$$

whose truncation error is $(6/5!)h^4 f_1^{(5)}$. Similar to Equation (1), a next-to-boundary scheme can be formulated as

$$f'_{j-1} + af'_j + \sigma f'_{j+1} = \frac{1}{h}(bf_{j-1} + cf_j + df_{j+1} + ef_{j+2} + ff_{j+3}), \tag{4}$$

where coefficients a to f are determined by

$$a = \frac{12+2\sigma}{3}, \qquad b = \frac{-(37+\sigma)}{12}, \qquad c = \frac{6-11\sigma}{9},$$
$$d = 3+\sigma, \qquad e = \frac{-2+\sigma}{3}, \qquad f = \frac{3-\sigma}{36}. \tag{5}$$

The truncation error is $[(\sigma-12)/360]h^5 f^{(6)}$, indicating 5th-order accuracy of the scheme. The combination of schemes (1) (denoted by ACS5), (4) (ACSBC5) and (3) (ACSBC4) should give a global formal accuracy of 5th order, denoted by ACS554.

In DNS, a fundamental requirement is to resolve *all* length scales in the turbulent flow. Thus, a finite-difference scheme's ability to resolve large wavenumbers is more relevant in this context than the order of accuracy measured by the truncation error in the Taylor-series expansion. The notion of *resolving power* or *resolution characteristics* was introduced by Lele [10] and re-emphasised by Adams and Shariff [9]. It is measured by the largest wavenumber k of a single wave e^{ikx} that can be accurately represented by the scheme on a given mesh. In most cases, the resolving power is correlated with the formal order of accuracy, but they are not exactly the same, as will be demonstrated below. By substituting e^{ikx} in (1), we may represent the approximation of the wavenumber k on a uniform mesh of unity length with cell width h by a modified wavenumber K

$$Kh = \frac{B\,\mathrm{e}^{-i2kh} + C\,\mathrm{e}^{-ikh} + D + E\,\mathrm{e}^{ikh} + F\,\mathrm{e}^{i2kh}}{i(\mathrm{e}^{-ikh} + A + \sigma\,\mathrm{e}^{ikh})}, \tag{6}$$

which is in general a complex number. The discrepancy between the real part of K and k is the dispersion error. The imaginary part of K introduces the dissipation error. In Figure 1, the dispersion and dissipation errors of compact inner and boundary schemes are compared with those of lower-order schemes. As can be seen, asymmetric compact schemes introduce numerical dissipation only at high wavenumbers, while low-order upwind schemes apply numerical dissipation over almost the entire wavenumber spectrum. Also, increasing asymmetry (decreasing σ) acts to increase numerical dissipation for the inner scheme ACS5, although the next-to-boundary scheme ACSBC5 does not follow the same trend. Compact symmetric schemes, as well as the 2nd-order central-difference scheme, have no numerical dissipation but only numerical dispersion. The advantages of compact schemes over the low-order explicit schemes are also obvious in terms of dispersion error. The latter can only resolve a very small range of wavenumbers on a given mesh and the 2nd-order schemes are no better than the 1st-order scheme. It is interesting to note that the 5th-order asymmetric scheme ACS5 with $\sigma = 0{\cdot}1$ is closer to the spectral solution over a wider range of the normalised wavenumber kh than the 6th-order symmetric scheme. In all cases, except the 4th-order boundary scheme, numerical dispersion of asymmetric schemes is not much worse than that of the symmetric scheme.

The development of a numerical scheme is incomplete without investigation of its stability. Unfortunately, the necessary and sufficient stability criteria for a general system of fully discretised Navier–Stokes equations with well-posed boundary conditions are unavailable. The usual practice is to test numerical stability separately on an advection equation (hyperbolic system) and a diffusion equation (parabolic system). Even in this case, rigorous proof of stability is an extremely difficult task [9, 15]. However, in temporal DNS, numerical discretisation

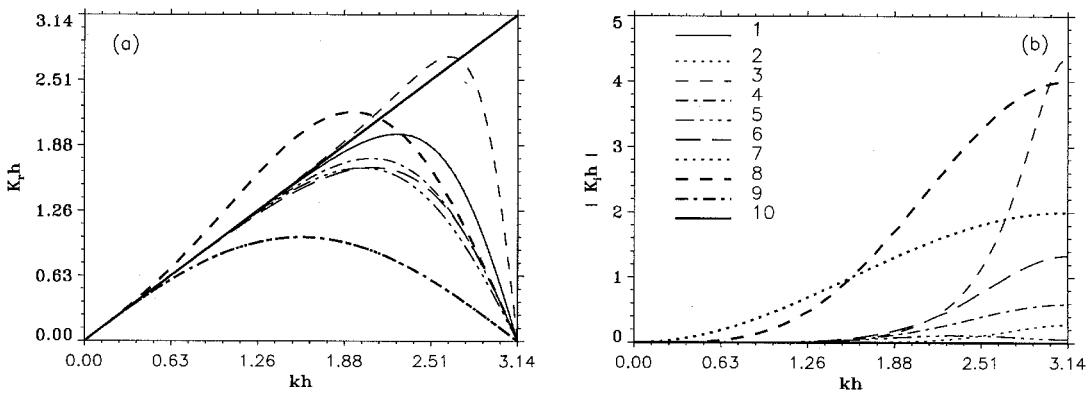

Figure 1. Resolution characteristics of finite difference schemes: (a) numerical dispersion and (b) numerical dissipation against the normalised wavenumber. (1) 6th-order symmetric compact scheme (ACS5, $\sigma = 1$); (2) 5th-order asymmetric compact scheme (ACS5, $\sigma = 0{\cdot}9$); (3) ACS5, $\sigma = 0{\cdot}1$; (4) 5th-order asymmetric compact next-to-boundary scheme (ACSBC5, $\sigma = 0{\cdot}1$); (5) ACSBC5, $\sigma = 0{\cdot}1$; (6) 4th-order asymmetric compact boundary scheme (ACSBC4); (7) 1st order explicit upwind scheme; (8) 2nd-order explicit upwind scheme; (9) 2nd-order explicit central scheme; (10) exact (spectral solution).

is accomplished by a *semi-discretisation* procedure in which spatial discretisation is applied first to a system of PDEs and the resulting system of discretised ODEs is then advanced in time with a method-of-lines approach. For semi-discretisation, it is much easier to derive stability conditions. Kreiss and Wu [16] have shown that under mild restrictions, a stable semi-discrete scheme leads to a stable fully discrete scheme if a locally stable Runge–Kutta method is used for time advancement. The stability of symmetric compact schemes has been thoroughly investigated in [11, 15] with the G-K-S theory [17]. The stability of two upwind-biased compact schemes has also been studied by Adams and Shariff [9]. In the following, we will carry out only limited stability analysis, while relying on the ultimate tests of actual numerical simulations in later sections. The analysis will focus on the *asymptotic stability*, since it is most relevant to integration over a very long time typical of DNS. Furthermore, only a scalar advection equation will be tested, since the asymmetric schemes are to be used only for the computation of the hyperbolic part of the Navier–Stokes equations. The asymptotic stability ensures that the integration will not blow up as time $t \to \infty$ on a given grid. The scalar advection equation is written as [9]

$$\frac{\partial u}{\partial t} + s\frac{\partial u}{\partial x} = 0, \quad 0 \leqslant x \leqslant 1, \quad 0 \leqslant t \leqslant \infty \tag{7}$$

with the boundary condition $u(0, t) = 0$ and the initial condition $u(x, 0) = f(x)$. A numerical scheme that is stable for $s > 0$ is said to be positively biased, while a scheme that is stable for $s < 0$ is said to be negatively biased.

To solve the scalar advection Equation (7), the domain [0, 1] is divided into $(N - 1)$ intervals of equal width h. The node points are x_j for $j = 0, 1, \ldots, N - 1$ and the function values at the nodes $u_j = u(x_j)$. With the spatial derivative $\partial u/\partial x$ replaced by a compact finite-difference scheme, a system of ODEs is obtained as

$$\frac{\mathrm{d}\boldsymbol{U}}{\mathrm{d}t} = -\frac{s}{h}P^{-1}Q\boldsymbol{U}, \tag{8}$$

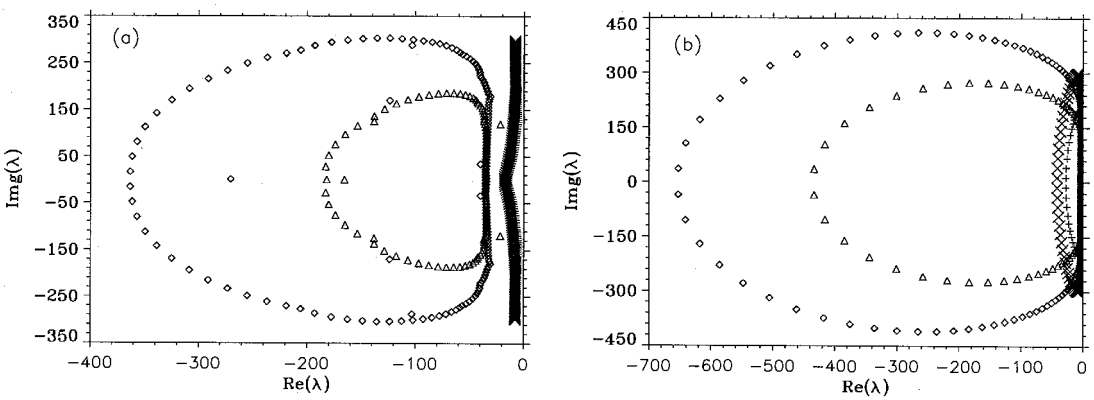

Figure 2. Eigenvalue spectra of the matrix $M = -(1/h)P^{-1}Q$, indicating stability of the asymmetric compact schemes. (a) scheme ACS554; (b) scheme ACS5 with period boundary conditions. +, $\sigma = 0{\cdot}9$, $N = 101$; ×, $\sigma = 0{\cdot}9$, $N = 151$; Δ, $\sigma = 0{\cdot}1$, $N = 101$; ◊, $\sigma = 0{\cdot}1$, $N = 151$.

where $\boldsymbol{U}$ is the function vector whose elements are $\{u_j\}$, and P and Q are matrices formed by the LHS- and RHS-coefficients of a compact scheme. The boundary condition is implemented at the node $j = 0$ $(u_0(t) = 0)$. A necessary condition for asymptotic stability is (see [15, 18]): "for a fixed grid with N nodes, the eigenvalues of the matrix $M = -(s/h)P^{-1}Q$ have negative real part or zero real part with a geometrical multiplicity of one". The eigenvalues λ are obtained by solution of the generalised eigenvalue problem

$$(M - \lambda I)\boldsymbol{V} = 0, \tag{9}$$

where $\boldsymbol{V}$ is the eigenvector and I the unit matrix.

We now test the compact schemes developed above. Without loss of generality, we let $s = 1$ in Equation (8). In Figure 2, the eigenvalues of M for scheme ACS554 and scheme ACS5 with periodic boundary conditions are shown for two different values of the mesh size N and the asymmetric parameter σ. In all cases, all eigenvalues are negative, although the eigenspectra are close to zero when σ is close to unity. Extensive tests have shown that all eigenvalues will stay negative if $-1{\cdot}0 < \sigma < 1{\cdot}0$, regardless of N. Therefore, ACS554 is asymptotically stable for $-1{\cdot}0 < \sigma < 1{\cdot}0$. It is thus positively biased. The inner scheme ACS5 with periodic boundary conditions is also asymptotically stable for $-1{\cdot}0 < \sigma < 1{\cdot}0$. Similarly, scheme ACSBC5 is also positively biased. By analogy, two negatively-biased compact schemes can be constructed: (i) a 5th-order inner scheme

$$\sigma f'_{j-1} + A^* f'_j + f'_{j+1} = \frac{1}{h}(B^* f_{j-2} + C^* f_{j-1} + D^* f_j + E^* f_{j+1} + F^* f_{j+2}) \tag{10}$$

with coefficients

$$\begin{aligned} A^* &= \frac{3(1+\sigma)}{2}, \qquad B^* = \frac{1-3\sigma}{24}, \qquad C^* = \frac{-(3+11\sigma)}{6}, \\ D^* &= \frac{3(-1+\sigma)}{2}, \qquad E^* = \frac{11+3\sigma}{3}, \qquad F^* = \frac{3-\sigma}{24}, \end{aligned} \tag{11}$$

and (ii) a 5th-order next-to-boundary scheme

$$\sigma f'_{j-1} + a^* f'_j + f'_{j+1} = \frac{1}{h}(b^* f_{j-1} + c^* f_j + d^* f_{j+1} + e^* f_{j+2} + f^* f_{j+3}) \tag{12}$$

with coefficients

$$a^* = \frac{12\sigma + 2}{3}, \qquad b^* = \frac{-(37\sigma + 1)}{12}, \qquad c^* = \frac{6\sigma - 11}{9},$$
$$d^* = 3\sigma + 1, \qquad e^* = \frac{-2\sigma + 1}{3}, \qquad f^* = \frac{3\sigma - 1}{36}. \tag{13}$$

It is emphasised here that the above procedure is just one method of testing the stability of linear equations. A stricter test is the ε-pseudo-eigenspectrum approach [19], which was used by Adams and Shariff [9] for upwind-biased compact schemes. Furthermore, asymptotic stability for semi-discrete schemes does not guarantee Lax stability [15], which requires boundedness of a numerical solution as the mesh is refined at a fixed time t, so that it converges to the true solution in the limit $h \to 0$. However, since these stability criteria do not readily generalise beyond the linear systems, we proceed to test the schemes with numerical simulations on the full Navier–Stokes equations.

The implementation of the asymmetric compact schemes is fairly straightforward. The efficient tridiagonal solver which we used for the symmetric compact schemes [12] can be employed directly for the present asymmetric schemes. Provided that $-1/3 < \sigma < 1$, the resulting matrices are diagonally dominant. Another convenience is the explicit control of numerical dissipation at the high wavenumbers via σ. The only penalty, compared with the symmetric schemes, is the additional computational cost required to determine the direction of the acoustic wave (sign of characteristic eigenvalues), according to which either a positively or a negatively stable asymmetric scheme is used.

Various values of the asymmetric parameter σ in the stable region have been used in test cases. We did not observe dramatic changes when going from one particular value to another, especially in the flow structures simulated. Mode energy of wavenumbers at the higher end of the spectrum does change with σ, but these wavenumbers are unimportant (as far as simulated flow features are concerned) in our *direct numerical simulations*, where high wavenumbers contain extremely low levels of energy. The main effect of the application of asymmetry ($\sigma < 1$) is that it allows simulations to go further into the regime with shocks, without spurious numerical oscillations arising. However, it should be noted that, even with the highest degree of asymmetry ($\sigma \to 0$), these compact schemes are not fully shock-capturing, since they are not conservative in general. Adams and Shariff [9] had to incorporate a conservative ENO scheme around discontinuities to make a non-conservative finite-difference scheme shock-capturing. The advantage of the asymmetric compact schemes developed here lies mainly in their ability to damp very high wavenumbers, while maintaining a high order of accuracy for other wavenumbers, allowing efficient and stable direct numerical solution of turbulent flow, possibly with weak shocklets. In a periodic direction, they could be used to replace Fourier methods, in which case the damping of high wavenumbers would effectively do the useful work of de-aliasing. In the present study, only weakly nonlinear processes have been simulated, so that even low levels of asymmetry ($\sigma \to 1$) have had the desired effects. In Section 3.2, computations with the value $\sigma = 0{\cdot}8$ are presented. Results of Section 4 have been checked with different values of σ to ensure accurate and consistent solutions. Since steep gradients in each case are predominantly in the r-direction, the mixed higher-order finite-difference/Fourier method is found to be sufficiently accurate up to the nonlinear stages

considered. Simulations beyond these are likely to be limited by the Fourier method, which in the future should be replaced by the asymmetric schemes developed here.

2.2. A MULTIDOMAIN APPROACH

The governing equations have a singularity at the jet axis $r = 0$, which presents a special numerical difficulty when cylindrical coordinates are used. Verzicco and Orlandi [20] avoided the problem by solving for the flux ru_r, instead of u_r, on a staggered grid using a finite-volume approach. In the present finite-difference method, we avoid the singularity by laying the meshlines close to, but not on the axis. A further complication around the axis arises due to the viscous stability condition at low Reynolds numbers. If uniform grids are used in the azimuthal direction, the very small grid spacing around the axis requires an extremely small time step. We may appreciate this by looking at the time-step formula, obtained for a model convection-diffusion equation, for the explicit time-advancement scheme

$$\Delta t = \frac{CFL}{D_c + D_d}, \tag{14}$$

where

$$D_c = \pi c \left(\frac{1}{\Delta r} + \frac{1}{r\Delta\theta} + \frac{1}{\Delta z} \right) + \pi \left(\frac{|u_r|}{\Delta r} + \frac{|u_\theta|}{r\Delta\theta} + \frac{|u_z|}{\Delta z} \right),$$

$$D_d = \frac{\pi^2 \mu}{(\gamma - 1)\rho M^2 \,\mathrm{Re}\,\mathrm{Pr}} \left[\frac{1}{(\Delta r)^2} + \frac{1}{(r\Delta\theta)^2} + \frac{1}{(\Delta z)^2} \right],$$

where c is the local sound speed. The time step is computed for each cell and the smallest value is used for time advancement. As can be seen, when $(r\Delta\theta) \to 0$ around the axis, $\Delta t \sim (r\Delta\theta)^2 \to 0$.

One way of reducing the time-step constraint is to treat convective terms explicitly, but viscous terms implicitly. The penalty is that a large amount of additional data must be stored, which in the case of typical DNS puts a severe constraint on the computer memory. In this study, we adopt a multidomain approach, which divides the computational domain into an inner region around the axis and an outer region extending to the far field. The resulting grid is illustrated in Figure 3. Real grids used in the computations should look like this except that the first azimuthal gridline is much closer to the axis (typically $r_{\min} = 10^{-4}$). As can be seen, a smaller number of grid points in the azimuthal direction is used in the inner region as compared to the outer region. Time advancement is performed separately in the two regions and the interpolation from the inner grid to the outer grid is through Fourier transformations. Typically, the reduction in time step amounts to one order of magnitude, with the CFL number kept the same at around 2. The same approach can be extended to have an inner region, an intermediate region and an outer region to gain further in numerical efficiency.

In the radial direction, a non-uniform grid is introduced through grid concentration and stretching. In the shear layer around $r = 1$, gridlines are concentrated to resolve the steep gradients. In the outer region, gridlines are stretched to reduce the overall number of grid

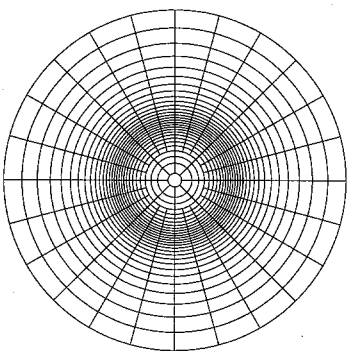

Figure 3. An illustration of a multi-domain computational grid (end view).

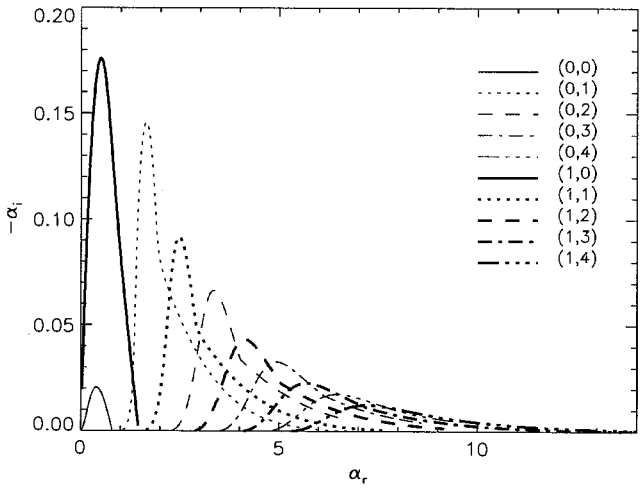

Figure 4. The spatial growth rate of vortical and acoustic instability modes for a Mach 3 jet.

points. However, gradients can also be large near the jet axis, so that a relatively fine grid is also needed there. A mapping function from uniform grid η to nonuniform grid r that concentrates mesh points around an arbitrary radial location $r = r_c$ on an interval $(0, L_r]$ is given by [21]:

$$r(\eta, r_c, b_r) = r_c \left\{ 1 + \frac{\sinh[b_r(\eta - S)]}{\sinh(b_r S)} \right\}, \tag{15}$$

where

$$S = \frac{1}{2b_r} \log \left[\frac{1 + (\mathrm{e}^{b_r} - 1)(r_c/L_r)}{1 + (\mathrm{e}^{-b_r} - 1)(r_c/L_r)} \right],$$

and b_r is a stretch parameter controlling the mesh distribution. To meet all the requirements described above, a linear combination of two mappings with different r_c and b_r is used as a final mesh.

The number of grid points in the three directions are denoted by N_r, N_θ and N_z. To improve numerical efficiency, interpolation algorithms are developed to increase or decrease N_r, N_θ or N_z, in response to the requirement of fully resolving the flow field. Fourier transformations are used for the θ- and z-directions, while a 7th-order B-spline interpolating algorithm [22] is employed for the r-direction. Usually, coarse meshes are used at the beginning of simulations, but finer and finer meshes are used to resolve more developed flow fields.

3. Linear stability analysis and code validation

3.1. Linear stability analysis

It is generally accepted that inviscid linear stability theory is sufficient to describe stability properties of free shear flows at high Reynolds numbers. The effects of viscosity is to damp disturbances at low Reynolds numbers. The growth rate of a disturbance deduced from inviscid theory provides, among other things, an upper limit for a viscous flow. In this study, an inviscid

linear stability analysis is carried out for validation of the new DNS code and to provide initial disturbances for round-jet simulations. We start the analysis with the Euler equations by dropping the viscous and heat-conduction terms from the Equations (31) to (35). A set of coupled first-order linearized equations for the six dependent variables $\Phi = u_r, u_\theta, u_z, \rho, p, T$ can be derived by the normal-mode, parallel-flow approach. Solutions of disturbances are sought in the following form:

$$\Phi'(r,\theta,z,t) = \widehat{\Phi}(r)\,\mathrm{e}^{i(\alpha z + m\theta - \omega t)}, \tag{16}$$

where α, m and ω are the axial wavenumber, azimuthal wavenumber and frequency, respectively. With some mathematical manipulation, the six linearized equations can be reduced to a single disturbance equation for pressure:

$$D^2\widehat{p} + AD\widehat{p} + B\widehat{p} = 0, \tag{17}$$

where $D \equiv \mathrm{d}/\mathrm{d}r$ and

$$A = \frac{1}{r} - D\log\overline{\rho} - \frac{2\alpha D\overline{U}_z}{\alpha\overline{U}_z - \omega} + \frac{1}{\mathrm{Fr}}\frac{i\alpha D\log\overline{\rho}}{(\alpha\overline{U}_z - \omega)^2}$$

$$B = \overline{\rho}M^2(\alpha\overline{U}_z - \omega)^2 - \alpha^2 - \frac{m^2}{r^2} - \frac{i\alpha\overline{\rho}M^2}{\mathrm{Fr}}$$

and Fr is the Froude number, which is a non-dimensional gravitational force. A bar over a variable indicates its mean value. The boundary conditions are:

$$\widehat{p}(r\to 0) = C_1 I_m(\beta r); \qquad \widehat{p}(r\to 0) = C_2 K_m(\beta r), \tag{18}$$

where I_m and K_m are the modified Bessel functions of the first and second kind of order m and

$$\beta^2 = \alpha^2 - \overline{\rho}M^2(\alpha\overline{U}_z - \omega)^2 + \frac{i\alpha\overline{\rho}M^2}{\mathrm{Fr}}. \tag{19}$$

Both the temporal (α real and ω complex) and spatial (α complex and ω real) stability problems are considered. The resulting eigenvalue problems for the pressure disturbance are solved by a two-domain shooting method, with integration by a variable-step fifth-order Runge–Kutta scheme [22]. In any case, β is complex and the Bessel functions I_m and K_m are computed by their Taylor series to convergence. The mean velocity is specified by a top-hat profile given by Michalke [23]:

$$\overline{U}_z = 0{\cdot}5\{1 + \tanh[0{\cdot}5R_z(1-r)]\}, \tag{20}$$

where the jet parameter $R_z \equiv R^*_{1/2}/\delta^*_m = 1/\delta_m$ characterises jet profiles at different axial positions. $R^*_{1/2}$ is the radius where $\overline{U}_z = 1/2$ and δ^*_m is the dimensional momentum thickness. The non-dimensionalisation is described in the Appendix. The mean temperature is calculated with a Crocco-Busemann relation for unity Prandtl number:

$$\overline{T} = M^2\frac{(\gamma-1)}{2}(\overline{U}_z(1+\overline{U}_2) - \overline{U}_z^2 - \overline{U}_2) + \frac{\overline{T}_2(1-\overline{U}_z)}{(1-\overline{U}_2)} + \frac{(\overline{U}_z - \overline{U}_2)}{(1-\overline{U}_2)}, \tag{21}$$

where subscripts 1 and 2 refer to the jet and the ambient free-stream conditions, respectively.

We now present the spatial linear stability results of a Mach-3 jet with stationary ambient. This is an interesting case owing to the presence of unstable modes of different characteristics. The Froude number is assumed to be infinity in the stability analysis and in subsequent numerical simulations. The mean velocity profile is given by Equation (20) with the jet parameter $R_z = 10$. The mean temperature is computed by Equation (21) with $\overline{T}_2 = 1$. Figures 4 and 5 show the spatial growth rate and phase speed of instability waves for the axisymmetric $(m = 0)$ and first helical $(m = 1)$ modes. These are plotted against the real part of the axial wavenumber, rather than the frequency, for greater clarity. At this Mach number, a spectrum of instability modes co-exist, but only the vortical mode and the first four acoustic modes are shown. To facilitate discussion, each mode (each curve in the figure) is designated by an integer pair (m, n), where m is the azimuthal wavenumber and n is an arbitrary number given to each continuous curve from left to right on the plot, starting with 0. Following Mack's [7] definition, modes (0, 0) and (1, 0) are called vortical modes, because they are a continuation of Kelvin–Helmholtz-instability modes into the supersonic regime. Modes with $n \geqslant 1$ only exist when there is an embedded region of locally supersonic flow relative to the phase speed of the instability wave and are called acoustic modes.

To describe the various modes better, relative Mach numbers for the jet and the ambient streams are defined respectively as:

$$M_{r1} = M\cos\phi\left(\overline{U}_1 - \frac{c_{ph}}{\cos\phi}\right), \qquad M_{r2} = \frac{M}{\overline{T}_2^{1/2}}\cos\phi\left(\frac{c_{ph}}{\cos\phi} - \overline{U}_2\right), \tag{22, 23}$$

where $\cos\phi = \alpha/(\alpha^2 + m^2/r^2)^{1/2}$ based on (16). A relative Mach number is a Mach number in the direction of a wave travelling at an angle ϕ relative to the z-axis with phase speed c_{ph}. A similar Mach number was defined by Mach [7] in a Cartesian coordinate system. When $M_{ri} > 1$ $(i = 1, 2)$, the wave is said to be supersonic relative to stream i. When $M_{ri} < 1$ $(i = 1, 2)$, the wave is said to be subsonic relative to stream i. For axisymmetric waves in a jet with $\overline{U}_2 = 0, \overline{T}_2 = 1$, the relative Mach numbers reduce to $M_{r1} = M(1 - c_{ph})$ and $M_{r2} = M c_{ph}$.

Experiments by Oertel [4, 5, 24] have shown that instability waves are most efficient in sound generation when their phase speeds are supersonic relative to the ambient fluid $(M_{r2} > 1)$. From the present linear stability analysis, it is seen that unstable waves with $M_{r2} > 1$, whether of acoustic or vortical origin, have oscillating pressure eigenfunctions that appear to be *radiating* into the far field. On the other hand, waves with $M_{r2} < 1$ have pressure eigenfunctions mainly confined to the jet. It is noted that in Figure 5 for acoustic modes there is a smooth transition from a non-radiating to a radiating regime, as the axial wavenumber becomes large. Therefore, one continuous curve in Figure 5 may contain two families of instability waves.

3.2. CODE VALIDATION

The DNS code in cylindrical coordinates developed in Section 2 is now validated against the linear stability theory (LST). Two types of tests are performed. In the first, the code is initialised with eigenfunctions from LST and run a few time steps at a high Reynolds number. The linear growth rates from LST and DNS should match. In the second approach, the code is initialised with random noise of small amplitude and run for a large number of time steps. The eigenfunctions developing from the DNS should match those from LST, if the same base

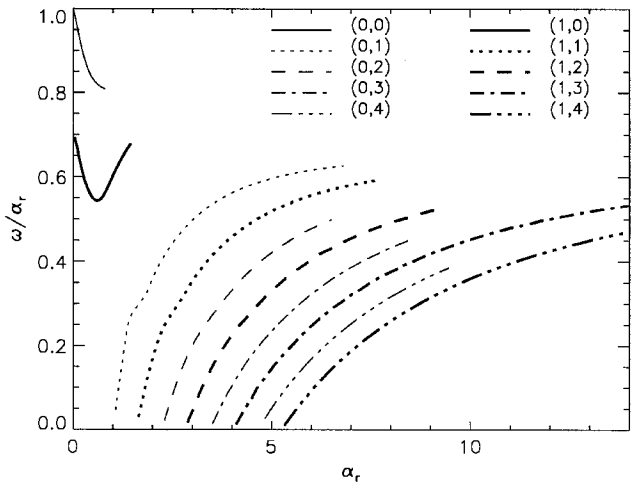

Figure 5. The phase speed of vortical and acoustic instability modes for a Mach 3 jet.

flow is used. To keep the base flow steady, forcing terms F_z and F_e are added to the LHS of the momentum Equation (34) and the energy Equation (35).

$$F_z = -\frac{\mathrm{d}}{\mathrm{d}r}\left(\frac{\overline{\mu}}{\mathrm{Re}}\frac{\mathrm{d}\overline{U}_z}{\mathrm{d}r}\right) - \frac{1}{r}\frac{\overline{\mu}}{\mathrm{Re}}\frac{\mathrm{d}\overline{U}_z}{\mathrm{d}r}, \tag{24}$$

$$F_e = -\frac{1}{(\gamma-1)M^2\mathrm{Pr}}\left[\frac{1}{r}\frac{\partial}{\partial r}\left(r\frac{\mu}{\mathrm{Re}}\frac{\partial\overline{T}}{\partial r}\right)\right] - \frac{\mathrm{d}}{\mathrm{d}r}\left(r\overline{U}_z\frac{\overline{\mu}}{\mathrm{Re}}\frac{\mathrm{d}\overline{U}_z}{\mathrm{d}r}\right), \tag{25}$$

where $\overline{U}_z$ is computed with (20) and $\overline{T}$ with (21) and $\overline{\mu} = \overline{T}^{0{\cdot}76}$. The forcing terms for other governing equations are zero.

In both methods, the following relations exist between Equation (16) of LST and the DNS data, when the temporal analysis is assumed to apply:

$$\omega_i = \frac{\mathrm{d}}{\mathrm{d}t}\log\{\mathrm{Real}[\Phi(k_z,k_\theta)]\}, \qquad \omega_r = \frac{\mathrm{d}}{\mathrm{d}t}\log\{\mathrm{Img}[\Phi(k_z,k_\theta)]\}, \tag{26, 27}$$

where $\Phi(k_z,k_\theta)$ are the Fourier coefficients of an arbitrary mode (k_z,k_θ) of any variable.

We have performed extensive tests of the first type, using eigenfunctions of various linear modes. The general conclusion is that values of ω_i and ω_r from the LST and the DNS have a perfect match as long as enough grid points in the r-direction are used. Typically, $N_r \sim 100$ for vortical modes and $N_r \sim 300$ for acoustic modes are found to be sufficient. Therefore, only tests of the second type will be detailed here, since they are more pertinent to long-time integration as used in DNS. The test conditions of two cases I and II are given in Table 1. The parameters are set on the basis of two instability waves from the LST in the previous section: a vortical, first helical mode (1, 0) at $M = 0{\cdot}8$ and the first acoustic, first helical mode $(1,\ 1)$ at $M = 3{\cdot}0$. The former has $\alpha = 1{\cdot}94$ and $\omega = 1{\cdot}09940252 - i0{\cdot}347208475$. The latter has $\alpha = 2{\cdot}508$ and $\omega = 0{\cdot}70320155 - i0{\cdot}0597658847$. The mean base flow and temperature are specified to be the same as in the LST. The computational box length L_z is chosen to be twice the fundamental wavelength $(2\pi/\alpha)$ in both cases. The Reynolds number Re has to be

Table 1. Test conditions for DNS to compute eigenfunctions from background random noise with amplitude Amp.

Case	mode (m, n)	Re	M	L_r	L_θ	L_z	N_r	N_θ	N_z	CFL	Amp	$t_{\max}$
I	(1, 0)	10^4	0·8	5·0	2π	6·478	201	4	8	2	10^{-7}	30
II	(1, 1)	10^5	3·0	5·0	2π	5·0	401	4	8	2	10^{-7}	130

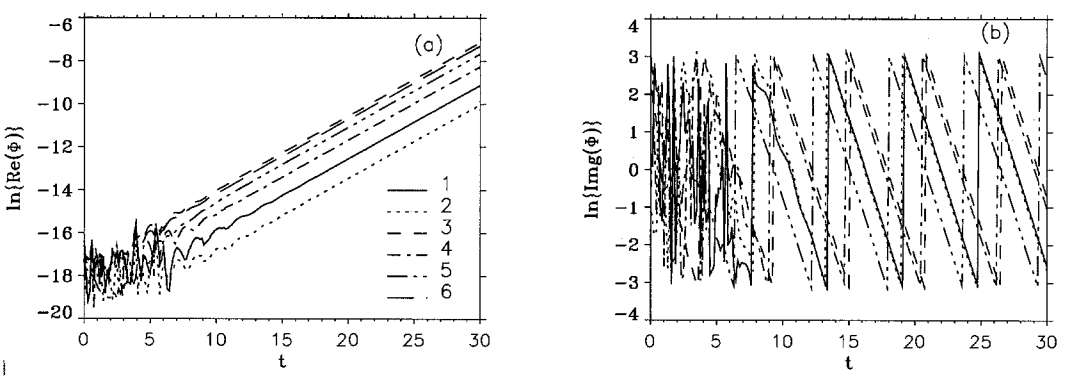

Figure 6. Temporal development of the Fourier coefficients of a vortical mode (1, 0) at $M = 0{\cdot}8$. (1) ρ; (2) T; (3) u_z; (4) u_r; (5) u_θ; (6) $\frac{1}{2}(u_z^2 + u_r^2 + u_\theta^2)$.

large enough, so that viscous effects are negligible to obtain inviscid results. The amplitude of the background noise must be small in order that the correct eigenfunctions evolve from the simulations before the flow becomes nonlinear.

The temporal development of the Fourier coefficients of various quantities is shown in Figure 6 for Case I. After an initial transient period, all quantities show linear development on this semi-log plot, corresponding to exponential growth in amplitude with time. Their growth rates are equal to each other (as evidenced by the parallel lines) and equal to ω_i from the LST. The jumps seen in Figure 6(b) at $\pm\pi$ are due to the periodicity of trigonometric functions. Apart from that, the temporal change in the imaginary part of the Fourier coefficients is linear, which gives the correct ω_r from the LST. The eigenfunctions of two velocity components extracted from Case I are compared with those from the LST in Figure 7, which shows excellent agreement after normalisation. No numerical instability is observed at the jet axis, nor any spurious wave reflections at the outer free boundary. All the observations above are also true for Case II, except that the correct eigenfunctions take a much longer time to evolve. The comparison of the axial velocity and temperature eigenfunctions with the LST is shown in Figure 8. Again, the agreement is excellent, even in regions with very steep gradients. It proves that the high-order asymmetric schemes are capable of resolving sharp gradients without spurious oscillations. On the whole, these tests show that the DNS code is accurate, stable and robust.

4. Direct simulation of a Mach-3 jet

To gain further understanding of the physics of the instability waves, it is helpful to investigate their nonlinear development and study the correspondence with experimental observations.

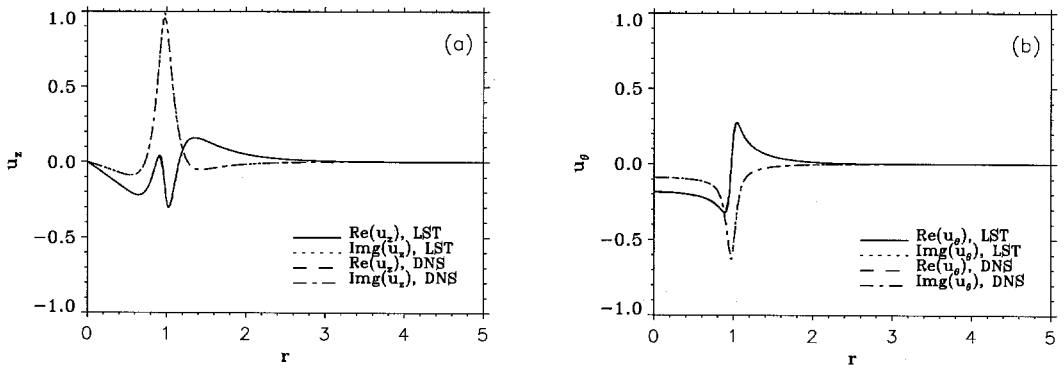

Figure 7. Comparison of eigenfunctions from the LST and the DNS ($t = 22$) of a vortical mode (1, 0) at $M = 0{\cdot}8$. (a) u_z; (b) u_θ.

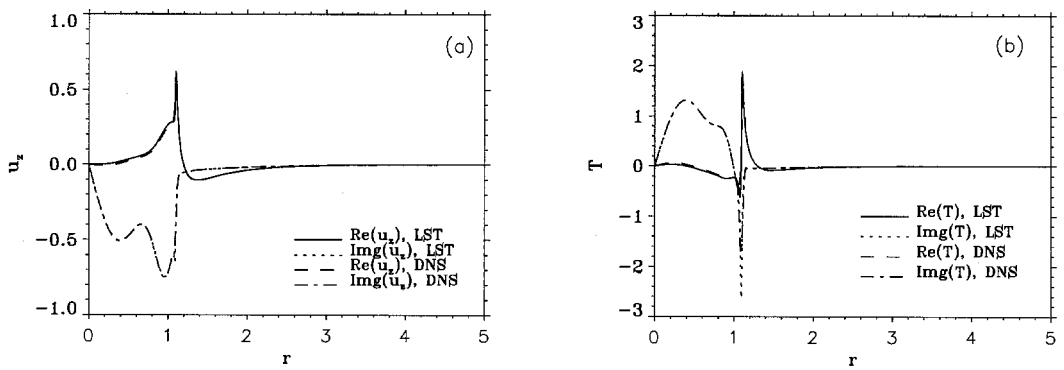

Figure 8. Comparison of eigenfunctions from the LST and DNS ($t = 120$) of an acoustic mode (1, 1) at $M = 3{\cdot}0$. (a) u_z; (b) T.

Direct simulations were thus performed with initial disturbances deduced from the LST described in the previous section. In all the simulations, the mean velocity and temperature profiles were initially specified the same as in the linear stability analysis. However, the forcing terms were not invoked, so that the jet mixing thickness could grow. The Reynolds number, based on the jet centreline velocity and the radius $R^*_{1/2}$, was 2000, so that viscous effects were included. Mesh size varied with simulation, but the maximum was $N_r \times N_\theta \times N_z = 601 \times 32 \times 144$. In Section 4.1 we consider the flow structures that arise from the unstable linear disturbances when applied separately, and in Section 4.2 we study nonlinear interactions between the different classes of disturbances.

4.1. Flow structures

Experimental observations of Oertel [4, 5] have shown the presence of three distinct classes of waves in supersonic jet flows. These waves, denoted by W', W and W'', are distinguished by having different convective velocities, satisfying the relation $U_{W'} > U_W > U_{W''}$. Furthermore, the two waves W' and W have acoustic near fields, with the wave angle of the latter larger than that of the former. The W'' wave has no acoustic near field, but displays a characteristic cross-hatched pattern within the jet. Tam and Hu [6] have provided an explanation

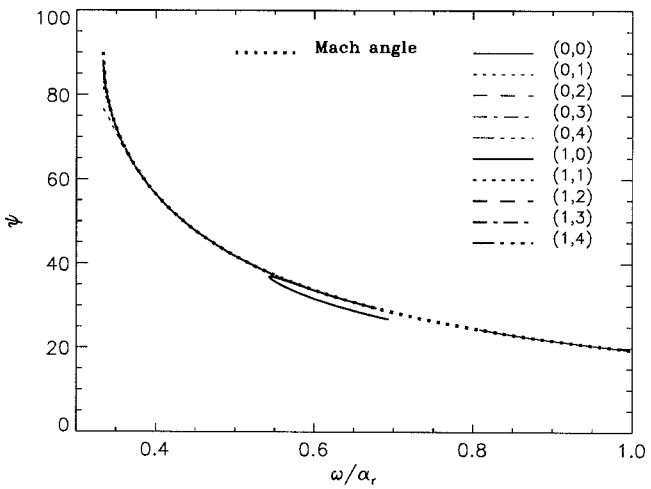

Figure 9. Wave angles of acoustic and vortical radiating instability modes compared with the Mach wave angles.

of these waves, using a linear stability theory, but they excluded nonlinear effects such as shock wave structures from their study. In Oertel's experiments, a special moving-frame-film technique was deployed to obtain stationary pictures of individual waves, which one might expect to be able to reproduce in a temporal DNS. To this end we have carried out separate simulations for each class of instability waves identified in our LST of the previous section. We note that the wave angle of a disturbance ψ outside the jet can be predicted by our linear theory in the limit $r \to \infty$ and Fr $\to \infty$:

$$\psi = \tan^{-1}\left(\frac{\alpha_r}{\beta_i}\right), \qquad \beta = \pm\alpha\sqrt{1 - \overline{\rho}M^2(\omega/\alpha)^2}. \tag{28}$$

The wave angles of all acoustic and vortical modes obtained in the previous section are shown in Figure 9. The wave angles of all modes collapse virtually onto one single curve against the wave phase speed. This curve is the Mach angle, given by $\psi_{\text{Mach}} = \sin^{-1}(1/M_{ph})$, where M_{ph} is equal to the disturbance phase speed divided by the ambient sound speed, and shown on the plot with a thick dotted line. A direct implication of this is that an instability wave travelling with a higher phase speed will radiate at a shallower angle to the horizontal than one travelling at a slower speed. This is in agreement with Oertel's experimental findings.

The first simulation uses the most unstable vortical, first helical wave at Mach 3. It has a wavenumber $\alpha = 0{\cdot}58$ and a phase speed $\omega_r/\alpha = 0{\cdot}55$. A computational box of normalised length $2\pi/\alpha = 10{\cdot}8$ is used so as to contain a fundamental wavelength. In a round jet, a single helical mode would produce a single helix. Since there is no preference in the boundary conditions for a helix with one sign of twist over the other, the simulation includes both the (1, 0) and $(-1,\ 0)$ modes, corresponding to the superposition of helical modes with the same amplitude, but opposite signs of twist. Figure 10 shows the pressure field developed from the original disturbance, with only half of the jet plotted for greater clarity. One sees pressure minima in the cores of a vortex and pressure maxima between vortices. The near-field wave pattern is weak in this case, although we see some preference for the structure outside the jet to have an angle of about 36°. This angle can be compared with the Mach angle predicted for waves travelling at the original phase speed which is 37°, indicating that the linear result

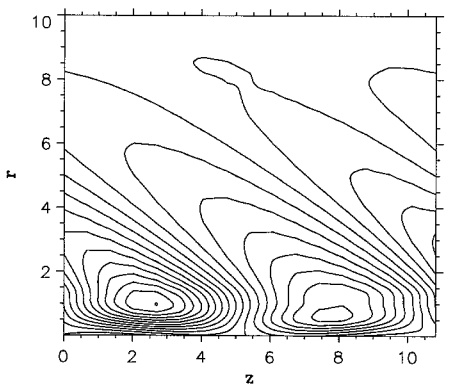

Figure 10. Pressure field developing from the most unstable vortical helical modes (1, 0) and $(-1,\ 0)$ $(t = 28{\cdot}0)$.

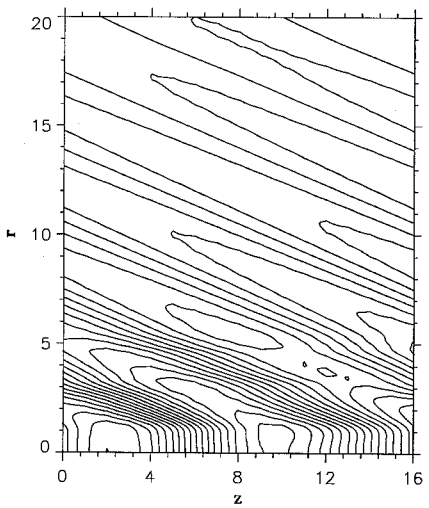

Figure 11. Pressure field developing from the most unstable vortical axisymmetric mode $(0,\ 0)$ $(t = 12{\cdot}0)$.

for the phase speed carries over into the nonlinear regime for the convective velocity. To reproduce the strong acoustic near field of the W' family of waves in Oertel's experiments, another simulation is conducted with the most unstable vortical axisymmetric wave with a wavenumber $\alpha = 0{\cdot}39$ and a phase speed $\omega_r/\alpha = 0{\cdot}85$. The pressure field is shown in Figure 11, showing the characteristic acoustic near field observed by Oertel. The dominant wave angle observed is 24°, in good agreement with the theoretical Mach wave angle of 23° for a wave moving at the original phase speed. It is now clear that the W' family of waves is due to the vortical instability waves with supersonic phase speeds. Also, axisymmetric vortical modes seem to be more closely associated with the acoustic field than the helical modes. However, the growth rates of axisymmetric vortical modes are much smaller than those of helical vortical modes.

Simulations with the various acoustic helical modes of peak growth rates (for each acoustic number n) have also been performed. Since the results are similar, only the case with the third acoustic modes $(1,\ 3)$ and $(-1,\ 3)$ is presented in Figure 12, in which the pressure field in two azimuthal planes are shown. The salient feature is the cross-hatched pattern confined within the jet. A near-field wave pattern is not observed. This would correspond to Oertel's W'' family of instability waves. By examining the dilatation field in the same planes in Figure 13, we find that the cross-hatched pattern consists of strong negative dilatation regions, which indicates that the steep gradients are shock waves. By looking at the flow patterns in other azimuthal planes, we find that the shock structures are highly three-dimensional. The original linear waves used in the simulation have a wavenumber of $\alpha = 5{\cdot}71$ and a phase speed of $\omega_r/\alpha = 0{\cdot}22$. Therefore, these are waves that are subsonic relative to the ambient $(M_{r2} < 1)$. They are always confined within the jet and are internal waves. When they are neutral, they correspond to sound waves reflecting back and forth within the core of the jet and are called Mack modes.

The other family of waves that have an acoustic near field cannot be found with modes of the peak growth rates predicted by the LST. Instead, we look at acoustic waves that are

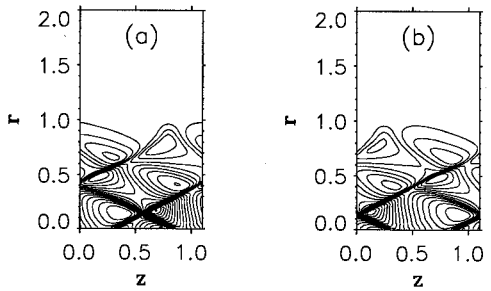

Figure 12. Pressure field developing from acoustic, non-radiating helical modes (1, 3) and $(-1,\ 3)$ $(t = 5{\cdot}0)$. (a) $\theta = 0$; (b) $\theta = \pi$.

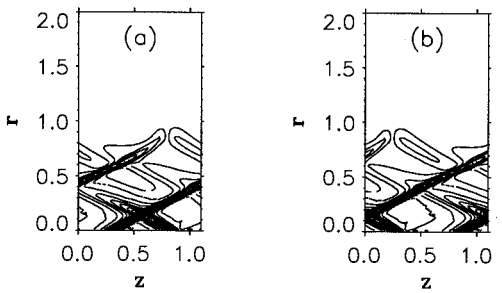

Figure 13. Dilatation field developing from acoustic, non-radiating helical modes (1, 3) and $(-1,\ 3)$ $(t = 5 \cdot 0)$. Solid lines indicate negative dilatation; dotted lines indicate positive dilatation. (a) $\theta = 0$; (b) $\theta = \pi$.

supersonic relative to the ambient $(M_{r2} > 1)$. Figure 14 shows the wave pattern of an acoustic axisymmetric disturbance from mode (0, 1). The wavenumber of the initial disturbance is $\alpha = 3{\cdot}43$ and the phase speed $\omega_r/\alpha = 0{\cdot}53$. The computational box contains four fundamental wave lengths. The pressure contours show an acoustic field with a dominant wave angle of about 41°, which from the definition of the Mach angle gives a phase speed of approximately $0 \cdot 51$. Again, the weakly nonlinear results from the simulations show only small departures from the linear results. This wave angle suggests that the wave corresponds to Oertel's W class of unstable disturbances, but we should note that selection of the wavenumber for the initial mode is somewhat arbitrary. We should also note that these modes exist over a range of phase speeds from 1/3 up to 2/3 and that the phase speeds overlap with those of the strongly unstable helical vortical modes. Nevertheless, it seems clear that Oertel's W class of waves is due to acoustic modes identifiable by the LST, which are continuations of the acoustic internal modes into the supersonic-phase-speed regime where they become radiating.

In Oertel's experiments [4, 5, 24], the three families of waves were found to have three preferred phase speeds, given by

$$U_W = \frac{c_2}{(c_1 + c_2)} U_1, \qquad U_{W'} = \left(1 + \frac{1}{M}\right) U_W, \qquad U_{W''} = \left(1 - \frac{1}{M}\right) U_W, \tag{29}$$

where c_1 and c_2 are sound speeds of the jet and ambient fluids, respectively. In [5], a three-layer hypothesis was proposed to explain the observed phenomena. In our present case of $M = 3$, these preferred speeds would be $U_{W'} = 2/3, U_W = 1/2$ and $U_{W''} = 1/3$. The first two speeds correspond to Mach angles 30° and 42°, respectively. Looking back at the simulations, we see that only the preferred speed and wave angle of the W family are closely reproduced in the simulation with the acoustic supersonic modes, but this is purely by coincidence of the choice of initial conditions, as explained earlier. The preferred values for the W' family may also be reproduced if a wave with the correct phase speed is picked up from the vortical modes. The W'' family of waves with a speed of exactly 1/3 would be sound waves, reflecting within the jet as internal Mach waves. This physical picture corresponds well with the simulation results. However, the phase speeds of the most unstable subsonic acoustic modes are generally lower than 1/3 (the most unstable mode has a phase speed about $0 \cdot 3$). We have seen that, in general, the preferred wave speeds found by experiments do not correspond to the most

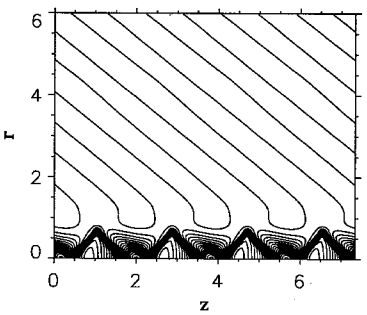

Figure 14. Pressure field developing from an acoustic, radiating, axisymmetric mode $(0,\ 1)$ $(t = 16{\cdot}0)$.

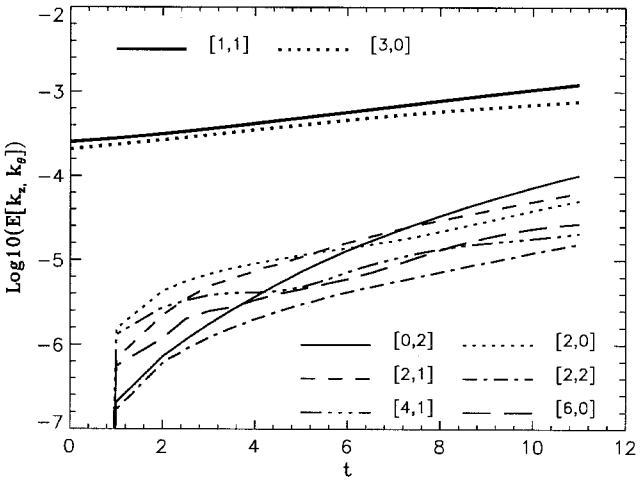

Figure 15. Temporal development of energy of combination modes due to weakly nonlinear interactions between the two most unstable waves at Mach 3.

unstable modes from our LST. The mechanism behind this cannot be revealed until further simulations are performed with sufficiently large boxes to accommodate more unstable waves, in which strongly nonlinear interactions among the waves might lead to some phase speed and angle preference.

4.2. NONLINEAR WAVE INTERACTIONS

A preliminary study has been made of the interactions between instability waves to investigate whether combinations of waves lead to new effects. The finite computational box obviously places a limit on the type and number of instability waves that could be included. Nevertheless, up to six instability waves were included in the simulations, leading to complex interactions. Three simulations (cases A, B and C) were performed with different combinations of initial disturbances.

In Case A the interaction between the two most dominant instability waves at Mach 3 is studied. These are the first helical vortical mode and the first acoustic axisymmetric mode with wavenumbers of $\alpha(1,\ 0) = 0{\cdot}571$ and $\alpha(0,\ 1) = 1{\cdot}714$ respectively. Choosing a box length L_z to fit the longest wavelength disturbance gives a length of $11{\cdot}0$, with room for three of the shorter waves. The wavenumber is chosen so that integer wavelengths can fit into the computational box exactly and satisfy the periodic streamwise boundary condition. The growth of energy in the eight most energetic modes is shown in Figure 15. The integrated mode energy is defined by

$$E[k_z, k_\theta] = \int_0^\infty u_i(k_z, k_\theta) u_i^\dagger(k_z, k_\theta)\, \mathrm{d}r, \tag{30}$$

where square brackets have been used to distinguish the modes for a specific simulation from the LST modes discussed in the previous sections. Here, k_z for a LST mode with a wavenumber α is $L_z\alpha/2\pi$; k_θ is equal to the azimuthal wavenumber m in the LST; $u_i(k_z, k_\theta)$ are the Fourier coefficients of velocity components and $\dagger$ indicates a complex conjugate.

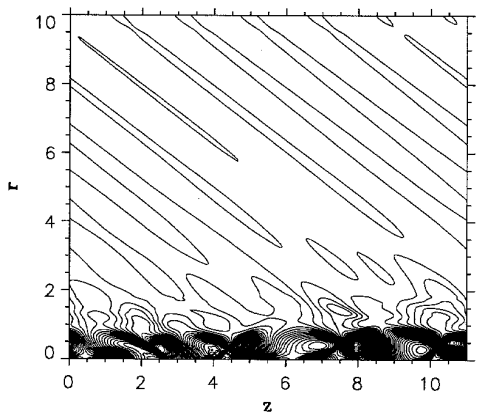

Figure 16. Pressure field developing from nonlinear interactions of multiple instability waves.

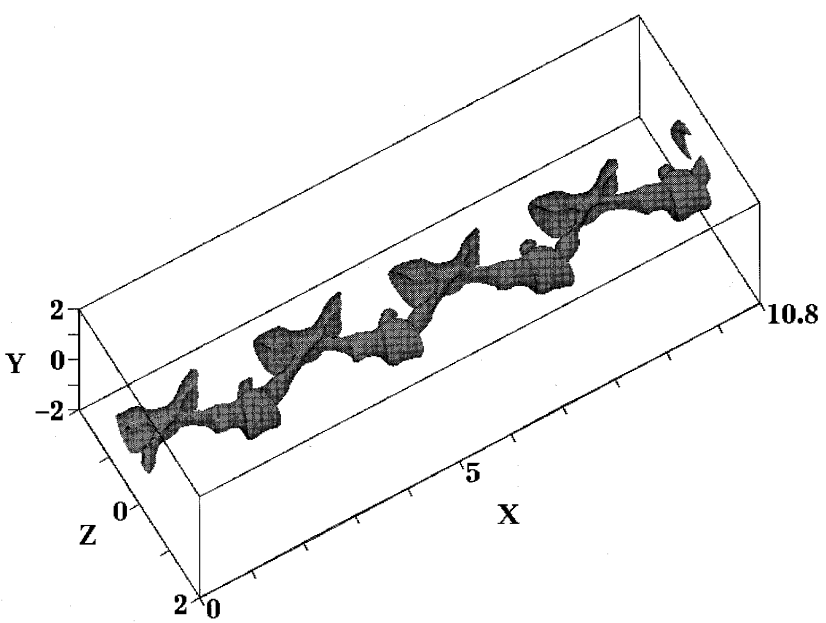

Figure 17. Isosurface of negative dilatation created by multiple helical instability waves, showing three-dimensional cross-hatched internal shock structures.

The modes that were introduced at the beginning of the simulation are the $[1,\ 1], [1,\ -1]$ (helical, nonradiating vortical) and [3, 0] (axisymmetric, nonradiating acoustic) modes. From the figure it can be seen that the combination modes ($[0,\ 2], [2,\ 0], [4,\ 1]$ etc.) develop rapidly due to weakly nonlinear wave interactions. As in many transition simulations the $[0,\ 2]$ mode, corresponding to the development of streamwise vortex structures, is the largest of the new modes that evolve, although in the time of the simulation it did not overtake the energy of the original waves. Other modes not predicted by the weakly nonlinear interaction were also observed to grow due to amplification of initial roundoff errors. However these modes did not grow to significant amplitudes during the simulation. Of the two main modes it appears that during the nonlinear evolution the $[1,\ 1]$ mode continues to grow, while the growth of the $[3,\ 0]$

mode levels off. This indicates that either the acoustic mode is nonlinearly stabilised by the presence of the vortical mode, or that it saturates out at a lower amplitude. More simulations are needed to clarify this issue.

Cases B and C were run primarily to check the flow structures appearing from combinations of several initial waves. In Case B we used an initial condition consisting of the modes [1, 1], $[1, -1]$, $[3, 0]$, $[4, 1]$, $[4, -1]$, and [6, 0]. The first three waves were the same as in Case A. The other three were from the most unstable acoustic helical mode and an axisymmetric acoustic supersonic/radiating mode. Case C consisted of the three most unstable helical modes $[1, 1]$, $[1, -1]$, $[4, 1]$, $[4, -1]$, $[8, 1]$ and $[8, -1]$. Visualisations from cases B and C are shown in Figure 16 (pressure contours) and Figure 17 (isosurface of negative dilatation), respectively. In Case B, a complex pattern of internal shock waves is formed due to wave interactions. In the meantime, a distinctive acoustic field is also developed. By tracking the movements of the individual structures, we find that the initial linear wave speeds have been altered by nonlinear effects. It is not clear whether such effects would ultimately lead to certain preference as observed in Oertel's experiments. In Case C, we see a three-dimensional cross-hatched pattern inside the jet, indicating the presence of internal shock waves. Such structures would be difficult to visualise by early experimental techniques, but confirmation by future experiments would be quite interesting.

5. Conclusions

Numerical methods have been developed to perform direct numerical simulation (DNS) and linear stability analysis of compressible jet flow in cylindrical coordinates. A multi-domain approach has been adopted in the DNS code to improve stability and efficiency in the presence of the singularity at the jet axis. A class of fifth-order asymmetric compact finite-difference inner and next-to-boundary schemes have been formulated and implemented. These schemes have explicit control of numerical dissipation at high wavenumbers and the resulting matrices are easily solved by any tridiagonal solver. The stability, accuracy and efficiency of the new DNS code have been validated against the linear stability theory (LST) and confirmed in full simulations. No spurious wave reflections have been observed at the jet origin or the outer free boundary, with the use of non-reflecting characteristic boundary conditions.

Three families of instability waves have been found by the LST at jet Mach number 3. These can be classified into vortical, supersonic/radiating acoustic and subsonic/non-radiating acoustic modes. Direct simulations in which these modes are used as initial conditions separately lead to three distinctive wave patterns that correspond to earlier experiments. The first two modes produce two types of acoustic near fields with different wave angles, whose relative magnitudes agree qualitatively with experimental observations. The third mode leads to the development of a cross-hatched internal shock wave structure, without an acoustic near field. Simulations with different combinations of these modes into the weakly nonlinear regime create highly complex wave patterns that resemble experimental visualisations. The initial wave speeds seem to be altered to some extent by nonlinear interaction effects, but the wave speed and angle preferences observed in experiments cannot be reproduced due to the limited computational domain. In all cases, the wave radiation angle and the phase speed are strongly correlated through the Mach angle, which collapses the LST results of all modes with supersonic phase speeds.

Acknowledgements

The work was funded by the UK Engineering and Physical Sciences Research Council under grant GR/H 40518.

Appendix A: Governing equations

The non-dimensional equations for the conservation of mass, momentum, energy and a passive scalar in the cylindrical coordinates (r, θ, z) are

$$\frac{\partial \rho}{\partial t} = -\frac{1}{r}\frac{\partial}{\partial r}(r\rho u_r) - \frac{1}{r}\frac{\partial}{\partial \theta}(\rho u_\theta) - \frac{\partial}{\partial z}(\rho u_z), \tag{A1}$$

$$\begin{aligned}\frac{\partial \rho u_r}{\partial t} &= -\frac{1}{r}\frac{\partial}{\partial r}[r(\rho u_r^2 + p)] - \frac{1}{r}\frac{\partial}{\partial \theta}(\rho u_r u_\theta) - \frac{\partial}{\partial z}(\rho u_r u_z) \\ &\quad + \frac{1}{r}\frac{\partial}{\partial r}(r\tau_{rr}) + \frac{1}{r}\frac{\partial \tau_{r\theta}}{\partial \theta} + \frac{\partial \tau_{rz}}{\partial z} + \frac{\rho u_\theta^2}{r} + \frac{p}{r} - \frac{\tau_{\theta\theta}}{r},\end{aligned} \tag{A2}$$

$$\begin{aligned}\frac{\partial \rho u_\theta}{\partial t} &= -\frac{1}{r}\frac{\partial}{\partial r}(r\rho u_\theta u_r) - \frac{1}{r}\frac{\partial}{\partial \theta}(\rho u_\theta^2 + p) - \frac{\partial}{\partial z}(\rho u_\theta u_z) \\ &\quad + \frac{1}{r}\frac{\partial}{\partial r}(r\tau_{\theta r}) + \frac{1}{r}\frac{\partial \tau_{\theta\theta}}{\partial \theta} + \frac{\partial \tau_{\theta z}}{\partial z} - \frac{\rho u_\theta u_r}{r} + \frac{\tau_{\theta r}}{r},\end{aligned} \tag{A3}$$

$$\begin{aligned}\frac{\partial \rho u_z}{\partial t} &= -\frac{1}{r}\frac{\partial}{\partial r}(r\rho u_z u_r) - \frac{1}{r}\frac{\partial}{\partial \theta}(\rho u_z u_\theta) - \frac{\partial}{\partial z}(\rho u_z^2 + p) \\ &\quad + \frac{1}{r}\frac{\partial}{\partial r}(r\tau_{zr}) + \frac{1}{r}\frac{\partial \tau_{z\theta}}{\partial \theta} + \frac{\partial \tau_{zz}}{\partial z},\end{aligned} \tag{A4}$$

$$\begin{aligned}\frac{\partial E_T}{\partial t} &= -\frac{1}{r}\frac{\partial}{\partial r}[r(E_T + p)u_r] - \frac{1}{r}\frac{\partial}{\partial \theta}[(E_T + p)u_\theta] - \frac{\partial}{\partial z}[(E_T + p)u_z] \\ &\quad + \frac{1}{(\gamma - 1)M^2 \mathrm{Pr}}\left[\frac{1}{r}\frac{\partial}{\partial r}\left(r\frac{\mu}{\mathrm{Re}}\frac{\partial T}{\partial r}\right) + \frac{1}{r^2}\frac{\partial}{\partial \theta}\left(\frac{\mu}{\mathrm{Re}}\frac{\partial T}{\partial \theta}\right) + \frac{\partial}{\partial z}\left(\frac{\mu}{\mathrm{Re}}\frac{\partial T}{\partial z}\right)\right] \\ &\quad + \frac{1}{r}\frac{\partial}{\partial r}[r(\tau_{rr}u_r + \tau_{r\theta}u_\theta + \tau_{rz}u_z)] + \frac{1}{r}\frac{\partial}{\partial \theta}[\tau_{\theta r}u_r + \tau_{\theta\theta}u_\theta + \tau_{\theta z}u_z] \\ &\quad + \frac{\partial}{\partial z}[\tau_{zr}u_r + \tau_{z\theta}u_\theta + \tau_{zz}u_z],\end{aligned} \tag{A5}$$

$$\begin{aligned}\frac{\partial \rho \xi}{\partial t} &= -\frac{1}{r}\frac{\partial}{\partial r}(r\rho\xi u_r) - \frac{1}{r}\frac{\partial}{\partial \theta}(\rho\xi u_\theta) - \frac{\partial}{\partial z}(\rho\xi u_z) \\ &\quad + \frac{1}{\mathrm{Sc}}\left[\frac{1}{r}\frac{\partial}{\partial r}\left(r\frac{\mu}{\mathrm{Re}}\frac{\partial \xi}{\partial r}\right) + \frac{1}{r^2}\frac{\partial}{\partial \theta}\left(\frac{\mu}{\mathrm{Re}}\frac{\partial \xi}{\partial \theta}\right) + \frac{\partial}{\partial z}\left(\frac{\mu}{\mathrm{Re}}\frac{\partial \xi}{\partial z}\right)\right],\end{aligned} \tag{A6}$$

where x_i $(i = r, \theta, z)$ are the radial, azimuthal and axial coordinates and u_i the corresponding velocity components. Further, ρ, p, T, t and μ are density, pressure, temperature, time and viscosity. The viscosity is computed by $\mu = T^{0.76}$. M, Re, Pr and Sc are the jet Mach number, Reynolds number, Prandtl number and Schmidt number; γ is the ratio of specific heats c_p/c_v; τ_{ij} $(i, j = r, \theta, z)$ is the viscous stress tensor for a Newtonian fluid. Finally, $E_T = \rho(e + u_i u_i/2)$ is the total energy, where e is the internal energy per unit mass. The non-dimensionalisation is performed with reference to the free-stream values of the jet (stream 1), as follows:

$$u_i = \frac{u_i^*}{U_1^*}, \qquad \rho = \frac{\rho^*}{\rho_1^*}, \qquad p = \frac{p^*}{\rho_1^* U_1^{*2}}, \qquad T = \frac{T^*}{T_1^*}, \tag{A7}$$

$$\mu = \frac{\mu^*}{\mu_1^*}, \qquad e = \frac{e^*}{U_1^{*2}}, \qquad t = \frac{t^* U_1^*}{R_{1/2}^*}, \qquad x_i = \frac{x_i^*}{R_{1/2}^*}, \tag{A8}$$

where the superscript $*$ indicates a dimensional quantity. $R_{1/2}^*$ is the jet radius where the axial velocity is equal to half the jet-centreline velocity.

References

1. S. K. Lele, Compressibility effects on turbulence. *Ann. Rev. Fluid Mech.* 26 (1994) 211–254.
2. N. D. Sandham and W. G. Reynolds, Three dimensional simulations of large eddies in the compressible mixing layer. *J. Fluid Mech.* 224 (1991) 133–158.
3. A. W. Vreman, N. D. Sandham and K. H. Luo, Compressible mixing layer growth rate and turbulence characteristics. *J. Fluid Mech.* 320 (1996) 235–258.
4. H. Oertel, Mach wave radiation of hot supersonic jets investigated by means of the shock tube and new optical techniques. In: A. Lifshitz and J. Rom (eds.), *Proc of the 12th Intl Symp. on Shock Tubes and Waves*, Jerusalem (1980) pp. 266–275.
5. H. Oertel, Coherent structures producing Machwaves inside and outside of the supersonic jet. In: R. Dumas and L. Fulachier (eds.), *Structure of Complex Turbulent Shear Flow.* Berlin: Springer (1983) pp. 334–343.
6. C. K. W. Tam and F. Q. Hu, On the three families of instability waves of high-speed jets. *J. Fluid Mech.* 201 (1989) 447–483.
7. L. M. Mack, On the inviscid acoustic-mode instability of supersonic shear flows. Part I: Two-dimensional waves. *Theor. and Comp. Fluid Dyn.* 2 (1990) 97–123.
8. A. W. Vreman, H. Kuerten and B. Geurts, Shocks in direct numerical simulation of the confined mixing layer. *Phys. Fluids* 7 (1995) 2105–2107.
9. N. A. Adams and K. Shariff, A high-resolution hybrid compact-ENO scheme for shock-turbulence interaction problems. *J. Comp. Phys.* 127 (1996) 27–51.
10. S. K. Lele, Compact finite difference schemes with spectral-like resolution. *J. Comp. Phys.* 103 (1992) 16–42.
11. N. A. Adams, An explicit temporal spectral/finite-difference method for the direct numerical simulation of compressible flat plate boundary layer transition, *DLR Report IB 221-92 A 25*. Göttingen: DLR, Germany (1992) 76pp.
12. K. H. Luo and N. D. Sandham, On the formation of small scales in a compressible mixing layer. In: P. R. Voke, L. Kleiser and J.-P. Chollet (eds.), *Fluid Mechanics and its Applications: Direct and Large-Eddy Simulation I*. Dordrecht: Kluwer Academic Publishers (1994) pp. 335–346.
13. K. W. Thompson, Time-dependent boundary conditions for hyperbolic systems, II. *J. Comp. Phys.* 89 (1990) 439–461.
14. B. Gustafsson, The convergence rate for difference approximations to mixed initial boundary value problems. *Math. Comput.* 29 (1975) 396–406.
15. M. H. Carpenter, D. Gottlieb and S. Abarbanel, The stability of numerical boundary treatments for compact high-order finite-difference schemes. *J. Comp. Phys.* 108 (1993) 272–295.
16. H.-O. Kreiss and L. Wu, On the stability definitions of difference approximations for the initial boundary value problem. *Appl. Num. Math.* 12 (1993) 213–227.
17. B. Gustafsson, H.-O. Kreiss and A. Sundström, Stability theory of difference approximations for mixed initial values problems II. *Math. Comput.* 26 (1972) 649–686.
18. H.-O. Kreiss and J. Lorenz, *Initial-Boundary Value Problems and the Navier-Stokes Equations*. New York: Academic Press (1989) 402pp.
19. S. C. Reddy and L. N. Trefethen, Stability of the method of lines. *Num. Math.* 62 (1992) 235–267.
20. R. Verzicco and P. Orlandi, A finite-difference scheme for three-dimensional incompressible flows in cylindrical coordinates. *J. Comp. Phys.* 123 (1996) 402–414.
21. D. A. Anderson, J. C. Tannehill and R. H. Pletcher, *Computational Fluid Mechanics and Heat Transfer.* New York: McGraw-Hill (1984) 599pp.
22. W. H. Press, B. P. Flannery, S. A. Teukolsky and W. T. Vetterling, *Numerical Recipes.* Cambridge: Cambridge University Press (1986) 818pp.
23. A. Michalke, Survey on jet instability theory. *Prog. Aerosp. Sci.* 21 (1984) 159–199.
24. H. Oertel, Mach wave radiation of hot supersonic jets. In: E. A. Muller (ed.), *Mechanics of Sound Generation in Flows*. Springer (1979) pp. 275–281.